

Development of 1.45-mm resolution four-layer DOI–PET detector for simultaneous measurement in 3T MRI

Fumihiko Nishikido · Atsushi Tachibana · Takayuki Obata ·
Naoko Inadama · Eiji Yoshida · Mikio Suga ·
Hideo Murayama · Taiga Yamaya

Received: 25 February 2014/Revised: 15 October 2014/Accepted: 15 October 2014/Published online: 28 October 2014
© Japanese Society of Radiological Technology and Japan Society of Medical Physics 2014

Abstract Recently, various types of PET–MRI systems have been developed by a number of research groups. However, almost all of the PET detectors used in these PET–MRI systems have no depth-of-interaction (DOI) capability. The DOI detector can reduce the parallax error and lead to improvement of the performance. We are developing a new PET–MRI system which consists of four-layer DOI detectors positioned close to the measured object to achieve high spatial resolution and high scanner sensitivity. As a first step, we are investigating influences the PET detector and the MRI system have on each other using a prototype four-layer DOI–PET detector. This prototype detector consists of a lutetium yttrium orthosilicate crystal block and a 4×4 multi-pixel photon counter array. The size of each crystal element is $1.45 \text{ mm} \times 1.45 \text{ mm} \times 4.5 \text{ mm}$, and the crystals are arranged in 6×6 elements \times 4 layers with reflectors. The detector and some electric components are packaged in an aluminum shielding box. Experiments were carried out with 3.0 T MRI (GE, Signa HDx) and a birdcage-type RF coil. We demonstrated that the DOI–PET detector was normally operated in simultaneous measurements with no influence of the MRI measurement. A slight influence of the PET detector on the static magnetic field of the MRI was observed near the PET detector. The signal-to-noise ratio

was decreased by presence of the PET detector due to environmental noise entering the MRI room through the cables, even though the PET detector was not powered up. On the other hand, no influence of electric noise from the PET detector in the simultaneous measurement on the MRI images was observed, even though the PET detector was positioned near the RF coil.

Keywords PET–MRI · PET detector · DOI detector · MPPC

1 Introduction

Recently, various types of PET–MRI systems have been developed by a number of research groups, and several PET–MRI scanners are now commercially available [1–15]. Almost all of the PET detectors used in these PET–MRI systems have no depth-of-interaction (DOI) capability, even though the systems have small-ring diameters to be used for rodent and human brain scanning [1–6, 9, 10, 14], except in three reports [7, 8, 13].

The small-ring-diameter PET scanner with the DOI–PET detector can realize high spatial resolution and high sensitivity. The closely placed detector positions of the small-ring diameter which reduce the influence of collinearity of the annihilation photons can achieve higher spatial resolution compared with large-ring PET scanners. In addition, the large solid angles of the small-diameter rings achieve a higher scanner sensitivity, compared with the large-diameter rings, especially in the case of the same axial length of the scanner. On the other hand, closely placed detector positions near the measured object increase the annihilation photons entering the scintillation crystals obliquely in the periphery of the field of view (FOV). The

F. Nishikido (✉) · A. Tachibana · T. Obata · N. Inadama ·
E. Yoshida · M. Suga · H. Murayama · T. Yamaya
Department of Biophysics Molecular Imaging Center, National
Institute of Radiological Sciences, 4-9-1 Anagawa, Inage-ku,
Chiba 263-8555, Japan
e-mail: funis@nirs.go.jp

M. Suga
Chiba University, 1-33 Yayoicho, Inage-ku,
Chiba 263-8522, Japan

oblique entry of the annihilation photons generally degrades the spatial resolution of the PET scanners without DOI capability (this is known as parallax error). On the other hand, the DOI-PET detector can suppress the parallax error and then realize a high sensitivity without degradation of the spatial resolution.

Based on these considerations, we have been developing an integrated PET-MRI system in which PET detectors with four-layer DOI capability are positioned close to the measured object so that high spatial resolution and high sensitivity are achieved. The four-layer DOI encoding method which we reported previously [16] can identify all four-layer crystals with photo-detectors attached to only one side of the crystal block. With this method, one can decrease the number of photo-detectors and their readout circuits which may influence on the MRI images in the PET-MRI, compared with other DOI detectors, such as dual-end readout [17, 18] and stack-type [19–21] DOI detectors.

As a first step, we investigated the reciprocal influences of the four-layer DOI-PET detector and the MRI system [22]. In this previous experiment, we used LGSO scintillation crystals whose size was $2.9 \text{ mm} \times 2.9 \text{ mm} \times 5.0 \text{ mm}$, and we are able to achieve a sufficient detector performance in simultaneous measurements with an MRI. To achieve higher spatial resolution, such as lower 1-mm imaging resolution, we changed the dimensions of the scintillation crystals to $1.45 \text{ mm} \times 1.45 \text{ mm} \times 4.5 \text{ mm}$. In addition, the scintillation material was changed from an LGSO crystal to a lutetium yttrium orthosilicate (LYSO) crystal, because the Gd included in the LGSO was magnetic material and the static magnetic field was distorted by the LGSO in the previous prototype detector.

We evaluated the performance of a prototype four-layer DOI detector using the $1.45 \text{ mm} \times 1.45 \text{ mm} \times 4.5 \text{ mm}$ crystals attached to a birdcage-type RF head coil in a 3.0 T MRI. In addition, we evaluated the influence of the four-layer DOI detector on the MRI image.

2 Materials and methods

A photograph of the prototype four-layer DOI-PET detector is shown in Fig. 1. The prototype four-layer DOI-PET detector consisted of an LYSO crystal block and a 4×4 multi-pixel photon counter (MPPC) array (S11064-050 series, Hamamatsu Photonics K.K.). The size of the crystal element was $1.45 \text{ mm} \times 1.45 \text{ mm} \times 4.5 \text{ mm}$. The crystals were arranged as 6×6 elements \times 4 layers with reflectors. The reflector arrangements in each layer are shown in Fig. 2a. RTV rubber (KE420, Shin-Etsu Chemical Co., Ltd.) was applied between the crystals, except for the spaces where the reflectors were inserted. Using this

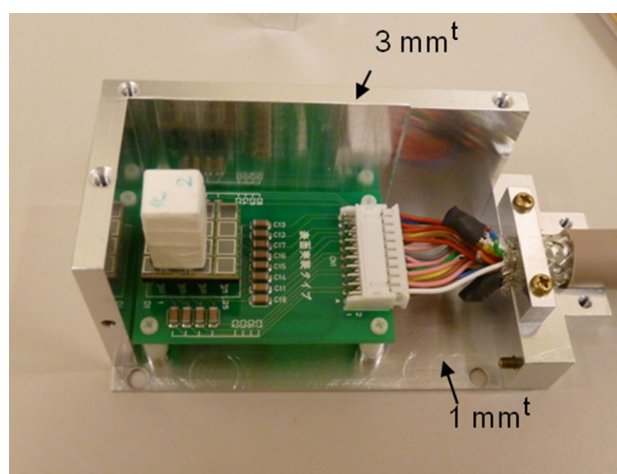


Fig. 1 Photograph of the prototype four-layer DOI detector used in the experiments

arrangement, we can represent crystal elements in all four layers on one position histogram, as shown in Fig. 2b. The crystal block had a minimum array size to demonstrate the practicality of the crystal identification performance of the four-layer DOI-PET detector. The details of the four-layer DOI encoding method are described in Ref. [16]. The readout pixels of the MPPC were $3 \times 3 \text{ mm}^2$, and they consisted of 50- μm cells. The crystal block was attached on 3×3 pixels, as shown in Fig. 3. The 50Ω terminations were applied for each MPPC. The detector and some electric components were packaged in a shielding box made of aluminum plates which was easier to make than the other materials. Because the thickness of the aluminum plates ranged from 1 to 3 mm, as shown Fig. 1, it was possible to achieve a higher shielding property than with shielding boxes made of thin shielding materials, such as copper foil or mesh. The shielding box was covered with aluminum foil ($\sim 100 \mu\text{m}$ thickness) for shielding of light entering through gaps between the aluminum plates. Almost materials in the DOI detectors, such as the scintillator block, MPPC array and aluminum shielding box, were non-magnetic to avoid any influence on the static magnetic field of MRI. However, the contact pins of the MPPC array, the sockets for them, a connector of signal cables, and some circuit elements may include magnetic materials.

Experiments were carried out with the 3.0 T MRI (GE, Signa HDx) and the birdcage-type RF coil (Fig. 4). The diameter of the RF coil was 30 cm. The shielding box with the detector and electric components was attached on the outside of the RF coil elements and inserted into the static magnetic field of the MRI. We placed an electric power supply for the MPPC and a data acquisition system outside the MRI room to reduce the influence of electric noise on the MRI performance; a schematic of the arrangement is shown in Fig. 5.

Fig. 2 a Reflector arrangement of the crystal block in the prototype DOI detector and b the ideal 2D position histogram for the reflector arrangement

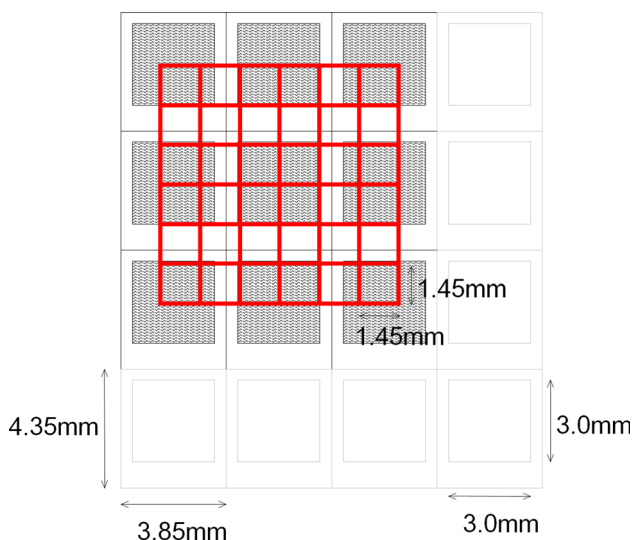
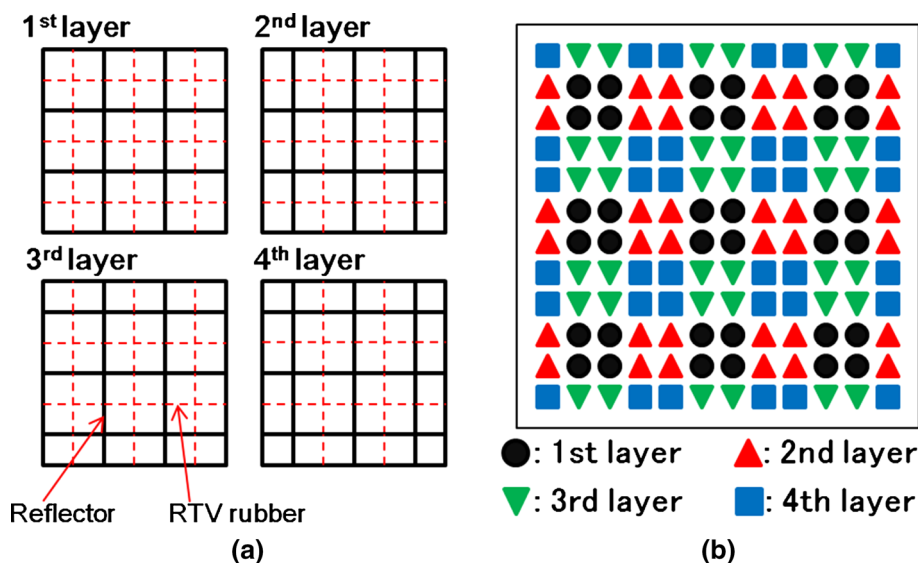


Fig. 3 Positional relationship of the $6 \times 6 \times 4$ LYSO crystal array and the MPPC pixels of the prototype detector. Gray-shaded areas show sensitive areas of the MPPCs. The seven white MPPCs were not used in the analysis

The data acquisition system consisted of a trigger system, amplifiers, and analog-to-digital converters (ADCs). The acquisition system was positioned outside the MRI room and connected to the MPPC array with 3-m-long cables through a gap at the door of the MRI room. The output signals passing through the 3-m-long cable from the MPPC are shown in Fig. 6. The shield of the cable was connected to the shielding box and the ground. The output signal from each MPPC channel was divided into two signals outside the MRI room. The first signal was individually recorded by the ADCs after passing through the amplifiers, and the other signal was used as a trigger signal. The trigger signal was generated by summation of the



Fig. 4 RF head coil and the four-layer DOI detector

divided signals from all 9 channels of the MPPC array with a leading edge discriminator (LED) and was finally fed into the ADCs as a gate signal generated with a gate generator.

Influences on the four-layer DOI-PET detector from the MRI were evaluated by comparison of position histograms and energy spectra obtained under three experimental conditions. First, the DOI detector was positioned outside the MRI room to obtain standard data. Second, the DOI detector was moved on the RF coil and evaluated without the MRI measurement. This meant that the DOI detector was affected only by the static magnetic field of the MRI. Finally, the simultaneous measurements of the DOI detector and the MRI were carried out for evaluation of the influence of the MRI measurement on the PET detector. The MRI was operated by the gradient-echo method ($TE = 5$ and 30 ms) during the data acquisition of the DOI detector. The two MRI sequences of the different TE

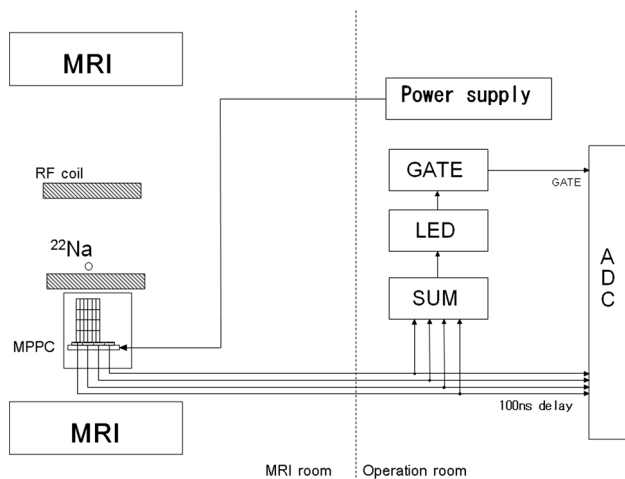
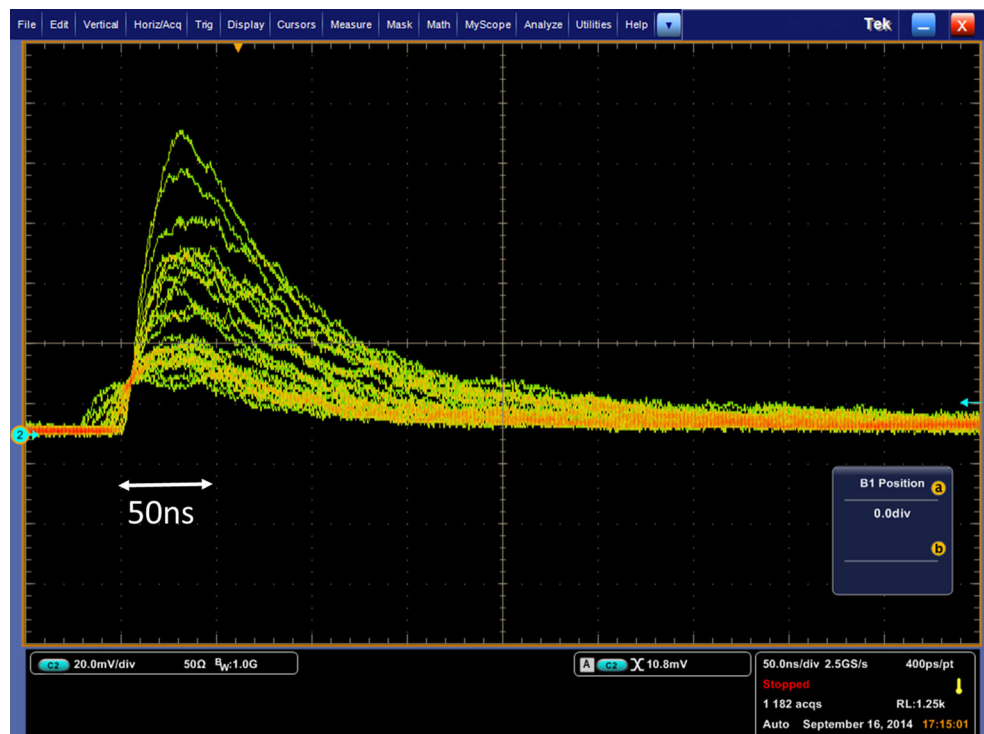


Fig. 5 Experimental setup for simultaneous measurements of the four-layer DOI-PET detector and the MRI

settings were operated sequentially in the simultaneous measurement. The MRI operations were used not only for evaluation of the PET detector performance in the simultaneous measurement but also for estimation of the uniformity of the static magnetic field at the same time. In all of the measurements, a ^{22}Na point source was positioned in front of the DOI-PET detector. The acquisition time was 5 min under each measurement condition. Temperature control and correction of variance of the MPPC gains were not applied. The operating voltage of the MPPC arrays was 72.48 V for all of the pixels.

Fig. 6 Signal after passing through the 3-m-long cable, measured with a digital phosphor oscilloscope



Next, the influence of the four-layer DOI-PET detector on the MRI images was evaluated. A 13-cm-diameter cylindrical phantom ($\text{CuSO}_4 \cdot 5\text{H}_2\text{O}$) was measured by the gradient-echo method. First, we obtained a phantom image without the DOI detector. In this measurement, no DOI detector components were in the MRI room, and the door of the MRI room was closed. In the second measurement, the PET detector was attached to the RF coil, and the power supply of the MPPC array was turned off. Under this experimental condition, the MRI was affected by the presence of the PET detector material. Finally, the MPPC was turned on, and simultaneous measurements of the PET detector and the MRI were carried out.

3 Results

3.1 Influence of the MRI on the four-layer DOI-PET detector

Figure 7 shows 2D position histograms for uniform irradiation of the ^{22}Na point source under the three experimental conditions: (a) outside the MRI room, (b) on the RF coil without MRI measurement, and (c) on the RF coil with MRI measurement. Only 511 keV photo-peak events are extracted and represented on these 2D position histograms. Each spot indicates interaction events in certain crystal elements. Crystals in the all layers can be clearly distinguished in the three position histograms. Non-uniformities

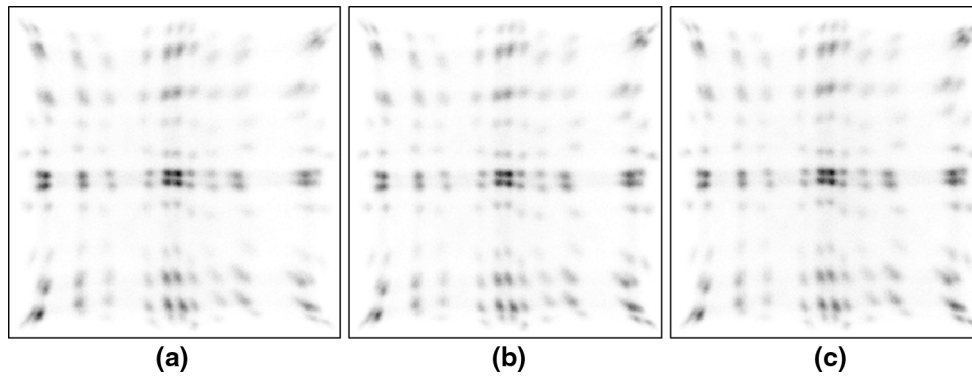


Fig. 7 Position histograms for uniform irradiation of 511 keV gamma rays in the three experimental conditions: **a** outside the MRI room, **b** on the RF coil without MRI measurement, and **c** on the RF coil with MRI measurement

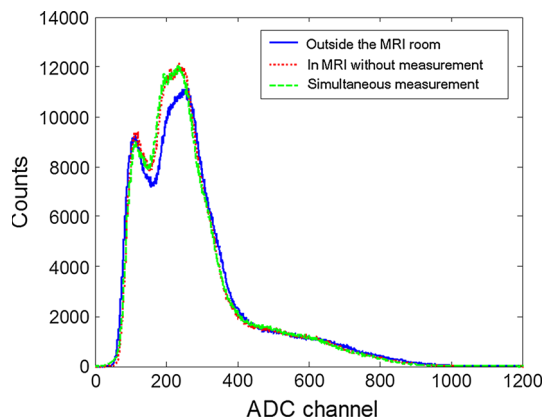


Fig. 8 Energy spectra for uniform irradiation of gamma rays from the ^{22}Na point source in the three experimental conditions, outside the MRI room, in the MRI without MRI measurement, and on the RF coil with MRI measurement (simultaneous measurement)

of the spot positions are caused by insensitive regions of the MPPC array. From comparison with the three position histograms, no degradation of the crystal identification performance was observed.

Figure 8 shows energy spectra for uniform irradiation of gamma rays from the ^{22}Na point source under the three experimental conditions: (a) outside the MRI room, (b) on the RF coil without MRI measurement, and (c) on the RF coil with MRI measurement (simultaneous measurement). Shoulders above 400 channels are caused by 1275 keV gamma rays from ^{22}Na . The insensitive areas of the MPPC array broaden the photo-peaks of the 511 keV gamma rays. The photo-peaks of the crystals on the insensitive areas are lower than those on the MPPC pixels due to loss of scintillation photons. Overlapping of the photo-peaks for the crystals on different positions of the MPPC leads to the broad photo-peaks of the spectra in Fig. 8.

Setting the region of interest on the position histograms, we obtained energy spectra for single crystal elements.

Examples of the energy spectra for single crystal elements in all four layers under the three experimental conditions are shown in Fig. 9. Photo-peaks of 511 and 1275 keV clearly appear for each energy spectrum. The ratios of the two photo-peak channels are ~ 2.4 and nearly equal to the ratio of the gamma ray energies of 2.50 ($=1.275/0.511$). This means that the linearity of the MPPC outputs around 511 keV is sufficient for evaluation of the energy resolution. Therefore, no saturation correction needs to be applied in the analysis of the energy resolution.

Tables 1 and 2 summarize the photo-peak positions and energy resolutions for 511 keV gamma rays. Although a shift of the pulse height of the PET detectors was observed, no significant degradation of the energy resolution was noted. This means that the reason for the peak shift of the energy spectra is not the influence of the MRI, but room temperature variation in the MRI room. The room temperature increased by approximately 1° during the experiment. Variation of the temperature around the PET detector slightly increases the temperature of the MPPCs and decreases the internal gains of the MPPCs. The several-percent decrease of the internal gain generally does not degrade the energy resolution. Therefore, we concluded that the MRI measurement did not influence the energy performance of the four-layer DOI-PET detector.

3.2 Influence of the DOI-PET detector on the MRI

Figure 10 shows MRI images obtained (a) without the PET detector, (b) with the PET detector (turned-off state), and (c) in the simultaneous measurement. Their signal-to-noise ratios (SNRs) were 36.8, 34.2, and 34.0, respectively. The SNR value did not change between the measurement with the PET detector turned off and the simultaneous measurement, compared with the measurement without the PET detector. This indicates that the electrical noises from the MPPC array, the data acquisition system, and the power

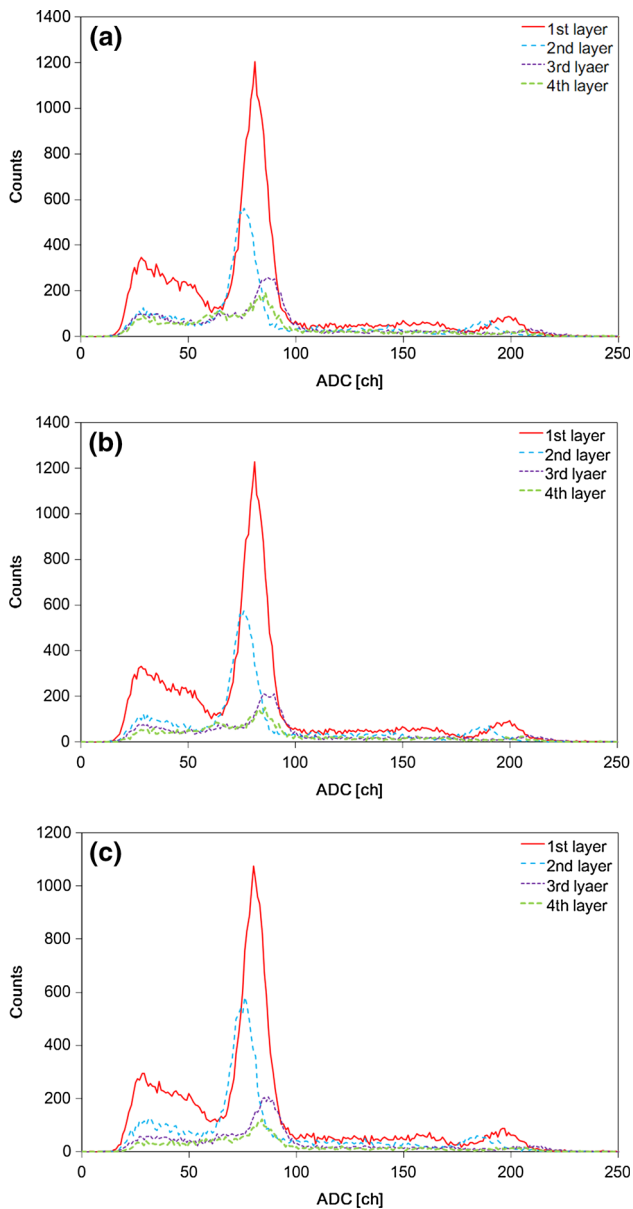


Fig. 9 Examples of energy spectra of single crystal elements in each layer for uniform irradiation of gamma rays from the ^{22}Na point source in the three experimental conditions: **a** outside the MRI room, **b** on the RF coil without MRI measurement, and **c** on the RF coil with MRI measurement

Table 1 Photo-peak positions for the single crystal elements (ch)

	Outside MRI room	MRI off	MRI on
1st layer	61.6 ± 13.5	58.4 ± 12.9	57.4 ± 12.9
2nd layer	63.2 ± 10.0	60.0 ± 9.5	59.0 ± 9.5
3rd layer	72.7 ± 11.4	69.1 ± 11.0	68.2 ± 11.0
4th layer	79.9 ± 13.6	77.6 ± 13.5	76.6 ± 13.5

Table 2 Energy resolutions for the single crystal elements (% FWHM)

	Outside MRI room	MRI off	MRI on
1st layer	21.1 ± 2.7	20.7 ± 2.7	21.6 ± 2.8
2nd layer	21.7 ± 2.7	21.8 ± 2.7	22.9 ± 3.0
3rd layer	21.7 ± 5.3	22.4 ± 5.5	23.2 ± 6.3
4th layer	22.6 ± 8.9	22.4 ± 9.1	22.9 ± 9.7

supplies were shielded well by the aluminum shielding box. On the other hand, the SNR was decreased from 36.8 to 34.2 by attachment of the PET detector, compared with Fig. 10a and b. It was caused by environmental noise entering the MRI room from outside the room through the cables.

To evaluate the influence of the PET detectors on the static magnetic field of the MRI, we calculated ΔB_0 maps with and without the PET detector. The ΔB_0 map shows the difference of the B_0 from the standard magnetic field in parts per million (ppm). The ΔB_0 maps were calculated from the two phase images of the cylindrical phantom by the gradient-echo method operated by two TEs ($TE = 5, 30$ ms) [23]. The ΔB_0 maps for the phantom positioned at the center of the FOV without and with the PET detectors are shown in Fig. 11a, b. Figure 11c shows the difference between the ΔB_0 maps without and with the PET detectors. The positions of the PET detector, the head coil elements, and the cylindrical phantom in this measurement are shown in Fig. 11d. The difference of the ΔB_0 maps is lower than ± 0.1 ppm. The ΔB_0 maps for the phantom near the PET detector without and with the PET detectors are shown in Fig. 12a, b. The difference between the ΔB_0 maps and the position relationship are also shown in Fig. 12c, d. The ΔB_0 dropped to ~ 1.0 ppm near the PET detector. The PET detector included some magnetic materials, such as the contact pins of the MPPC array and sockets for them, which were generally nickel coated. As a result, the static magnetic field was decreased by the presence of the PET detector.

4 Discussion and conclusion

We have proposed a new PET–MRI system of a birdcage-type RF coil integrated with PET detectors to realize high spatial resolution and sensitivity of the PET scanner using a four-layer DOI detector. As the first step, we constructed a prototype four-layer DOI–PET detector for the PET–MRI system and evaluated the reciprocal influence between the PET and MRI measurements with the commercial birdcage-type RF coil. As a result, we demonstrated that the DOI–PET detector operated normally in simultaneous

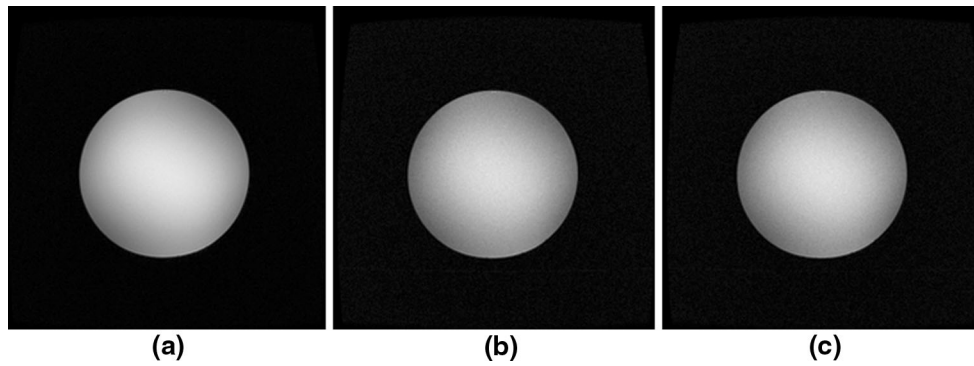


Fig. 10 Magnitude images. **a** Without the PET detector, **b** with the PET detector (turned-off state), and **c** in the simultaneous measurement

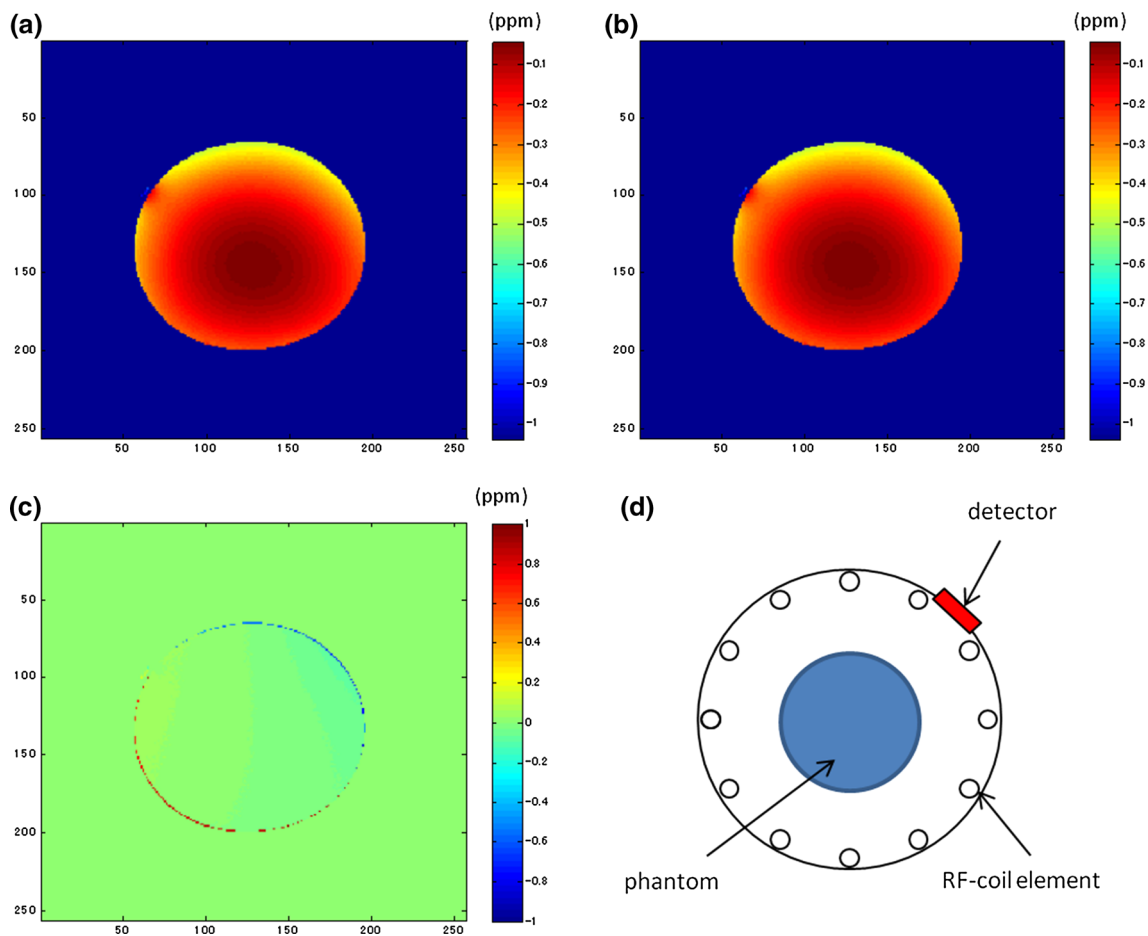


Fig. 11 ΔB_0 maps for the phantom positioned at the center of the FOV. **a** Without the PET detector and **b** with the PET detector (turned-off state). **c** Subtracted image between (a) and (b). **d** Positional relationship of the PET detector, cylindrical phantom, and RF coil elements

measurements of MRI with no influence from the MRI measurement. The influence of the PET detector on the static magnetic field of the MRI was observed, whereas no influence of noise from the electronics of the PET detector on the MRI images was obtained, even though the PET detector was positioned near the RF coil. On the other hand, some groups reported performance degradation of

PET detectors or MRI images in simultaneous measurements [24–27]. The primary reason for differences between these reports and the proposed system is the shielding methods of the PET detectors. Although we used the aluminum shielding box which had the sufficient thickness for noise reduction (>1 mm), they used thin copper foils or no shielding. As a result, there was no influence on the SNR of

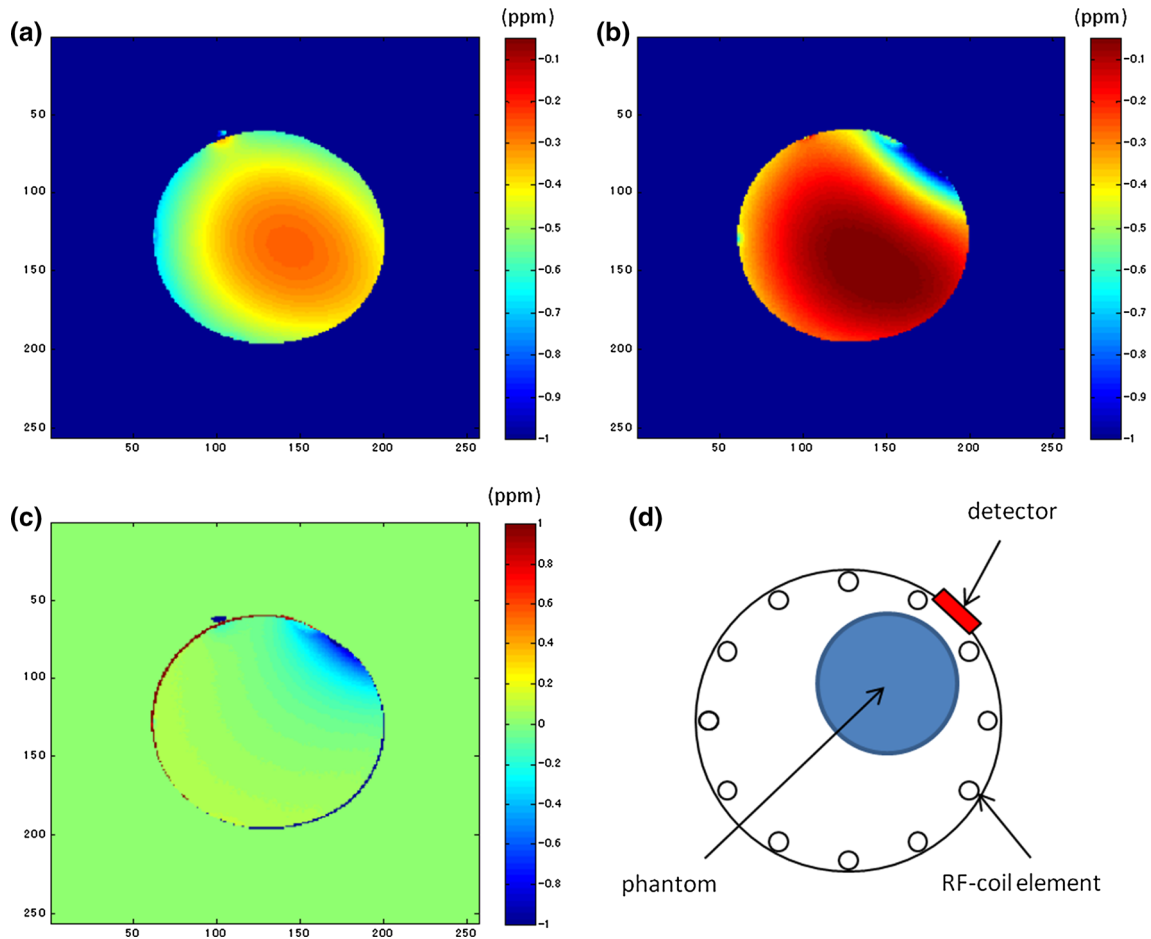


Fig. 12 ΔB_0 maps for the phantom positioned near the PET detector position. **a** Without the PET detector and **b** with the PET detector (turned-off state). **c** Subtracted image between (a) and (b). **d** The positional relationship of the PET detector, cylindrical phantom, and RF coil elements

the MRI image from the PET detector and on the PET signals from the RF pulse of the MRI.

However, the large volume of the shielding material may increase the eddy current by field gradient pulses, compared with the shielding by a copper foil. It is possible to cause artifacts in some kinds of MRI sequences, such as N half artifact in echo-planar imaging [28, 29]. We are evaluating the shielding performance and the influence of the eddy current for various shielding materials. We will change the shielding material to a material that achieved the best performance.

We expect that the performance of the PET-MRI system can be improved by the following modifications: First, removal of magnetic materials in the PET detectors will suppress the influence on the static magnetic field of the MRI. The static magnetic field was decreased by the contact pins of the MPPC array and the sockets for them in the experiment, as shown in Fig. 12b. Use of surface-mounted MPPCs which have no contact pins, such as S11828-3344M, will improve the homogeneity of the static magnetic field. Second, decreasing the insensitive area of the

MPPC array will improve the performance of the PET detector, especially the energy resolution. Energy resolutions of the PET detector above 20 % are caused by scintillation light loss in the insensitive area of the MPPC array, because the energy resolution depends on the number of photons collected in each MPPC pixel. By use of an MPPC array with a small insensitive area, the energy resolution will be improved and can be achieved to be better than 20 %, and the crystal identification performance will also be improved. Finally, the use of an RF coil dedicated to the proposed PET-MRI will improve the quality of the MRI images. The dedicated RF coil tuned with the PET detectors can achieve a higher imaging performance, compared with the commercial RF head coil, which is not dedicated to the presented system.

As a next step, we are developing a one-ring prototype of the integrated PET-MRI system which consists of eight PET detectors and a prototype RF coil dedicated for PET-MRI. The prototype RF coil will be tuned with the PET detectors attached to the RF coil elements. In addition, surface-mount MPPCs which have a small insensitive area

between the MPPC pixels (e.g., S11828-3344M) will be used instead of the S11064-050 which was used in the present study. We expect that these modifications will improve the MRI images obtained and the performance of the PET detector in simultaneous measurements.

Acknowledgments Part of this work was supported by JSPS KAKENHI Grant No. 24390295 and funds from the Japan Science and Technology Agency (JST) for the project “Development of Systems and Technology for Advanced Measurement and Analysis”.

Conflict of interest The authors declare that they have no conflict of interest.

References

- Shao Y, Cherry S. Simultaneous PET and MR imaging. *Phys Med Biol.* 1997;42:1965–70.
- Slates RB, Farahani K, Shao Y, Marsden PK, Taylor J, Summers PE, et al. A study of artefacts in simultaneous PET and MR imaging using a prototype MR compatible PET scanner. *Phys Med Biol.* 1999;44:2015–27.
- Catana C, Wu Y, Judenhofer MS, Qi J, Pichler BJ, Cherry SR. Simultaneous acquisition of multislice PET and MR images: initial results with a MR-compatible PET scanner. *J Nucl Med.* 2006;47:1968–76.
- Grazioso R, Zhang N, Corbeil J, Schmand M, Ladebeck R, Vester M, et al. APD-based PET detector for simultaneous PET/MR imaging. *Nucl Instrum Methods A.* 2006;569:301–5.
- Pichler BJ, Judenhofer MS, Catana C, Walton JH, Kneilling M, Nutt RE, et al. Performance test of an LSO-APD detector in a 7-T MRI scanner for simultaneous PET/MRI. *J Nucl Med.* 2006;47:639–47.
- Schlyer D, Vaska P, Tomasi D, Woody C, Maramraju S-H, Southeikal S et al. A simultaneous PET/MRI scanner based on RatCAP in small animals. In: *IEEE nuclear science symposium conference record; 2007.* pp. 3256–3256.
- Yamamoto S, Hatazawa J, Imaizumi M, Shimosegawa E, Aoki M, Sugiyama E, et al. A multi-slice dual layer MR-compatible animal PET system. *IEEE Trans Nucl Sci.* 2009;56:2706–13.
- Yamamoto S, Imaizumi M, Kanai Y, Tatsumi M, Aoki M, Sugiyama E, et al. Design and performance from an integrated PET/MRI system for small animals. *Ann Nucl Med.* 2010;24:89–98.
- Kwon SI, Lee JS, Yoon HS, Ito M, Ko GB, Choi JY, et al. Development of small-animal PET prototype using silicon photomultiplier (SiPM): initial results of phantom and animal imaging studies. *J Nucl Med.* 2011;52:572–9.
- Maramraju SH, Smith SD, Junnarkar SS, Schulz D, Stoll S, Ravindranath B, et al. Small animal simultaneous PET/MRI: initial experiences in a 9.4 T microMRI. *Phys Med Biol.* 2011;56:2459–80.
- Zaidi H, Ojha N, Morich M, Griesmer J, Hu Z, Maniawski P, et al. Design and performance evaluation of a whole-body ingenuity TF PET-MRI system. *Phys Med Biol.* 2011;56:3091–106.
- Delso G, Fürst S, Jakoby B, Ladebeck R, Ganter C, Nekolla SG, et al. Performance measurements of the Siemens mMR integrated whole-body PET/MR scanner. *J Nucl Med.* 2011;52:1914–22.
- Yamamoto S, Watabe T, Watabe H, Aoki M, Sugiyama E, Imaizumi M, et al. Simultaneous imaging using Si-PM-based PET and MRI for development of an integrated PET/MRI system. *Phys Med Biol.* 2012;57:N1–13.
- Yoon HS, Ko GB, Kwon S II, Lee CM, Ito M, Chan Song I et al. Initial results of simultaneous PET/MRI experiments with an MRI-compatible silicon photomultiplier PET scanner. *J Nucl Med.* 2012;53:608–14.
- Wehner J, Weissler B, Dueppenbecker P, Gebhardt P, Schug D, Ruetten W et al. PET/MRI insert using digital SiPMs: investigation of MR-compatibility. *Nucl Instrum Methods A.* 2014;734:116–21.
- Tomoaki T, Murayama H, Kitamura K, Yamaya T, Yoshida E, Omura T, et al. A four-layer depth of interaction detector block for small animal PET. *IEEE Trans Nucl Sci.* 2004;51:2537–42.
- Shao Y, Li H, Gao K. Initial experimental studies of using solid-state photomultiplier for PET applications. *Nucl Instrum Methods A.* 2007;580:944–50.
- Yang Y, Dokhale PA, Silverman RW, Shah KS, McClish MA, Farrell R, et al. Depth of interaction resolution measurements for a high resolution PET detector using position sensitive avalanche photodiodes. *Phys Med Biol.* 2006;51:2131–42.
- Herbert DJ, Moehrs S, D’Ascenzo N, Belcari N, Del Guerra A, Morsani F, et al. The silicon photomultiplier for application to high-resolution positron emission tomography. *Nucl Instrum Methods A.* 2007;573:84–7.
- Lau FWY, Vandenbroucke A, Reynolds PD, Olcott PD, Horowitz MA, Levin CS. Analog signal multiplexing for PSAPD-based PET detectors: simulation and experimental validation. *Phys Med Biol.* 2010;55:7149–74.
- Omura T, Moriya T, Yamada R, Yamauchi H, Saito A, Sakai T et al. Development of a high-resolution four-layer DOI detector using MPPCs for brain PET. In: *IEEE nuclear science symposium conference record, 3560-3; 2012.*
- Nishikido F, Obata T, Shimizu K, Suga M, Inadama N, Tachibana A, et al. Feasibility of a brain-dedicated PET-MRI system using four-layer detectors integrated with an RF head coil. *Nucl Instrum Methods A.* 2014;756:6–13.
- Och JG, Clarke GD, Sobo WT, et al. Acceptance testing of magnetic resonance imaging systems: report of AAPM nuclear magnetic resonance task group No. 6. *Med Phys.* 1992;19:22025.
- Hong SJ, Song IC, Ito M, Kwon SI, Lee GS, Sim KS, et al. An investigation into the use of Geiger-mode solid-state photomultipliers for simultaneous PET and MRI application. *IEEE Trans Nucl Sci.* 2008;55:882–8.
- Woody C et al. Preliminary studies of a simultaneous PET/MRI scanner based on the RatCAP small animal tomography. *Nucl Instrum Methods A.* 2007; 571:102–5.
- Yamamoto S, Watanabe T, Watabe H, Aoki M, Sugiyama E, Imaizumi M, et al. Interference between PET and MRI sub-systems in a silicon-photomultiplier-based PET/MRI system. *Phys Med Biol.* 2011;56:4147–59.
- Huh YS, Choi Y, Hong KJ, Jung JH, Hu W, Kang JH, et al. Development of filtering methods for PET signals contaminated by RF pulses for combined PET-MRI. *IEEE Trans Nucl Sci.* 2013;60(5):3205–11.
- Jezzard P, et al. Characterization of and correction for eddy current artifacts in echo planar diffusion imaging. *MRM.* 1998;39:801–12.
- Shimizu K, Suga M, Nishikido F, Kuribayashi H, Nakajima I, Kawabata Y et al. Quantitative analysis of effect of shield boxes for PET electronics combined with an MR head coil. In: *IEEE nuclear science symposium conference record, M05-5; 2013.*